ARTICLES
https://doi.org/10.1038/s41929-020-00504-x

nature catalysis

Check for updates

Highly active and stable stepped Cu surface for enhanced electrochemical CO_2 reduction to C_2H_4

Chungseok Choi[1], Soonho Kwon[2], Tao Cheng[2,3], Mingjie Xu[4,5,6], Peter Tieu[7], Changsoo Lee[1,8], Jin Cai[1], Hyuck Mo Lee[8], Xiaoqing Pan[4,5,9], Xiangfeng Duan[10], William A. Goddard III[2]✉ and Yu Huang[1]✉

Electrochemical CO_2 reduction to value-added chemical feedstocks is of considerable interest for renewable energy storage and renewable source generation while mitigating CO_2 emissions from human activity. Copper represents an effective catalyst in reducing CO_2 to hydrocarbons or oxygenates, but it is often plagued by a low product selectivity and limited long-term stability. Here we report that copper nanowires with rich surface steps exhibit a remarkably high Faradaic efficiency for C_2H_4 that can be maintained for over 200 hours. Computational studies reveal that these steps are thermodynamically favoured compared with Cu(100) surface under the operating conditions and the stepped surface favours C_2 products by suppressing the C_1 pathway and hydrogen production.

Developing highly efficient electrocatalysts for the carbon dioxide reduction reaction (CO_2RR) to value-added fuels and chemicals offers a feasible pathway for renewable energy storage and could help mitigate the ever-increasing carbon dioxide (CO_2) emissions from human activities[1]. Several metal electrodes are known to catalyse CO_2RR in aqueous solutions[2]. Among the catalysts explored to date, copper (Cu) is the only electrocatalytic material that converts CO_2 into hydrocarbon products with a considerable activity and efficiency[3]. Additionally, owing to Cu's natural abundance[4,5] and low cost, it has been intensively studied for CO_2RR for decades[4,6–13]. However, the low product selectivity towards valuable fuel products and the lack of long-term stability remain major challenges for Cu-based catalysts[11,13]. Various approaches have been explored to address these challenges[6–18]. For example, Kanan and co-workers reported that the grain boundaries on Cu film[16,17] and surface defects[18] promote the production of hydrocarbons with one-carbon (C_1 product)[13] (~45% CO ca. −0.5 V and ~33% HCO_2H ca. −0.65 V versus the reversible hydrogen electrode (RHE), referenced to for all potentials in this article unless otherwise specified). Moreover, residual surface copper oxides[14,19,20] have been suggested to enhance the production of hydrocarbons with two carbons (C_2)[14].

Among the major gaseous products, ethylene (C_2H_4) is desirable as it is a basic building block to produce various plastics, solvents and cosmetics. In 2020 alone, 158 million tons of C_2H_4 global market is estimated, and the annual demand for C_2H_4 is expected to grow ~4.5% through to 2027[21]. However, the selective production of C_2H_4 from CO_2RR is challenging, with competition from the hydrogen evolution reaction (HER) and methane (CH_4) production[22]. It has been predicted and shown with single-crystal studies that the formation of specific surface step sites on Cu catalysts can lower the barrier for CO dimerization to promote C_2 production over C_1 products[23,24]. Indeed, Cheng et al. performed a thorough density functional theory (DFT) screening of active defect sites for electrochemical CO_2RR to C_2 products at grain boundaries of Cu nanoparticles (NPs)[23]. They found that the most active surface sites for C_2 production on grain boundaries consist of one strong CO binding site next to one weak CO binding site, which substantially reduces the energy of the *OCCHO transition state and makes it active towards C_2 products[23].

Here we report the preparation of Cu nanowires (CuNWs) with highly active stepped surfaces through the in situ electrochemical activation of pregrown CuNWs with {100} surfaces (Fig. 1). The electrochemical CO_2RR studies demonstrate a remarkably high C_2 selectivity with a Faradaic efficiency (FE) towards C_2H_4 ($FE_{C_2H_4} > 70\%$), as well as exceptionally high stability for ~200 hours. The high C_2H_4 selectivity is attributed to the unique surface structure of the CuNWs with abundant stepped sites. Our DFT studies showed that the Cu(511) plane [3(100)×(111)] stepped surface is thermodynamically favoured at CO_2RR conditions over either Cu(100) or Cu(111) under the operating conditions, which explains the experimentally observed long-term stability. The calculations also revealed a higher barrier for the C_1 path, along with a slower HER on Cu(511) compared with that of C_2, which leads to the greatly enhanced selectivity towards C_2H_4.

Results

Preparation of CuNWs with surface steps. The CuNWs were synthesized with a protocol similar to a previously reported approach[25], and the resulting CuNWs typically display a fivefold twin with

[1]Department of Materials Science and Engineering, University of California, Los Angeles, Los Angeles, CA, USA. [2]Department of Applied Physics and Materials Science, California Institute of Technology, Pasadena, CA, USA. [3]Institute of Functional Nano & Soft Materials (FUNSOM), Jiangsu Key Laboratory for Carbon-Based Functional Materials & Devices, Joint International Research Laboratory of Carbon-Based Functional Materials and Devices, Soochow University, Suzhou, P. R. China. [4]Irvine Materials Research Institute (IMRI), University of California, Irvine, Irvine, CA, USA. [5]Department of Materials Science and Engineering, University of California, Irvine, Irvine, CA, USA. [6]Fok Ying Tung Research Institute, The Hong Kong University of Science and Technology, Guangzhou, P. R. China. [7]Department of Chemistry, University of California, Irvine, Irvine, CA, USA. [8]Department of Materials Science and Engineering, Korea Advanced Institute of Science and Technology, Yuseong-gu, Republic of Korea. [9]Department of Physics and Astronomy, University of California, Irvine, Irvine, CA, USA. [10]Department of Chemistry and Biochemistry, University of California, Los Angeles, Los Angeles, CA, USA. ✉e-mail: wag@caltech.edu; yhuang@seas.ucla.edu

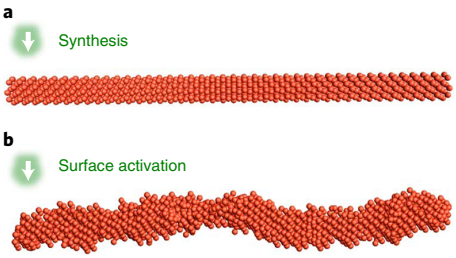

Fig. 1 | Schematic of preparing CuNWs with surface steps. a, The as-synthesized CuNWs with a {100} surface. **b**, The CuNWs are activated in situ during the electrochemical CO_2RR to form surface steps.

the <110> axial direction and {100} side facets (see Methods for details). The synthesized CuNWs (termed Syn-CuNWs) were collected by centrifuge and washed five times with a hexane/ethanol mixture. The structure of the Syn-CuNWs was characterized by powder X-ray diffraction, transmission electron microscopy (TEM) and secondary electron imaging (SEI). The powder X-ray diffraction peaks of Syn-CuNWs match those of Cu (Supplementary Fig. 1a). A low-resolution TEM image of the Syn-CuNWs demonstrates its one-dimensional wire structure with a smooth surface (Fig. 2a) and an average diameter of 25 ± 7.7 nm (Supplementary Fig. 1b). A high-resolution TEM (HRTEM) of the Syn-CuNWs (Fig. 2a inset) shows a 1.27 Å lattice spacing of Cu{220} and the Cu<110> direction, which is consistent with the expected <110> axial-growth direction of the Syn-CuNWs[25,26].

To generate surface steps, the Syn-CuNWs were subjected to an electrochemical activation in the environment similar to that of the CO_2RR, which was under a high reduction bias ($V = -1.05$ V) in 0.1 M $KHCO_3$ electrolyte solution for over 30 minutes. After this electrochemical activation, the activated CuNWs (termed A-CuNWs) showed highly uneven surfaces (Fig. 2b). HRTEM of A-CuNWs after one hour of activation showed zone $[01\bar{1}]$ of fast Fourier transform (FFT) spots. The plane spacing in zone $[01\bar{1}]$ of the FFT spots shows 2.08 Å, 1.80 Å and 1.27 Å, which were indexed as Cu{111}, Cu{200} and Cu{220}, respectively (Fig. 2c,d)[25,26]. Both the Cu_2O and Cu phases were found on the A-CuNW surface with the <110> axial direction and <100> towards the sides, which suggests a {100}-rich side surface (Fig. 2c and Supplementary Fig. 2). The Cu_2O observed in HRTEM on the surface of the A-CuNWs was probably due to the instant surface oxidation after removing the reduction potential[20], which will convert back to Cu under applied reduction potentials of about −0.8 to −1.1 V (ref. [27]). The HRTEM images on the A-CuNW surface also indicated the formation of surface steps, with some in the form of [n(100)×m(111)] (Fig. 2d and Supplementary Fig. 2).

In addition, SEI in the scanning transmission electron microscopy mode also confirmed a pronounced roughened or stepped topology of the A-CuNWs compared with that of the Syn-CuNWs (Supplementary Fig. 3). We further performed lead (Pb) under potential deposition[28] (Supplementary Fig. 4), which revealed that the electrochemical surface area (ECSA) of the A-CuNWs (3.07 $m^2 g^{-1}$) was higher than that of the Syn-CuNWs (1.68 $m^2 g^{-1}$). Thus, the electrochemical surface activation process produced A-CuNWs with stepped surfaces and with an increased ECSA. Moreover, electrochemical impedance spectroscopy showed that the A-CuNWs had a slightly lower ohmic resistance (42 Ω) than that of the Syn-CuNWs (45 Ω) (Supplementary Fig. 5).

Electrochemical characterization of CuNW surfaces. To further evaluate the surface features of the CuNWs, we examined OH^- adsorption spectra on the catalyst surface through the Cu ↔ Cu_2O redox reaction cyclic voltammetry (CV) (see Methods for details) (Supplementary Fig. 6). The Syn-CuNWs showed OH^- adsorption peaks at 0.362 and 0.395 V (Fig. 3a), which correspond to the Cu(OH) adsorption ($Cu(OH)_{ad}$) peaks on Cu{100} and Cu{110}, respectively[29–32]. In particular, the most pronounced $Cu(OH)_{ad}$ peak at 0.362 V corresponds well with the expected Cu{100} facet on the Syn-CuNW surface. Interestingly, compared with Syn-CuNWs, one additional OH^- adsorption peak emerged at 0.316 V (Fig. 3a) on A-CuNWs. This additional peak (assigned here to A-(hkl)) appeared at a more negative potential than those of the low-index facets of Cu, which indicates a stronger OH^- adsorption[33,34], which has been assigned to Cu surfaces with high-energy steps[31,35]. For example, Raciti et al. assigned an OH^- adsorption peak (~0.34 V), with a negative shift from the Cu{100} peak (~0.36 V), to Cu(211) ([3(111)×(100)]) (ref. [31]). DFT calculations of Cu–O binding energy by Tian and Wang also reported that the stepped surface of Cu(311) ([2(100)×(111)]) led to a stronger Cu–O binding energy compared with those of Cu(100) and Cu(111) (ref. [35]). To gain a more quantitative evaluation of the surface-facet evolution, we estimated the percentage of the surface planes on Syn-CuNWs and A-CuNWs by integrating each OH_{ad} peak after subtracting the background (Fig. 3b–e and Supplementary Fig. 7). The Syn-CuNW surface comprised mostly Cu{100} (67%) and Cu{110} (32%) (Fig. 3b), consistent with a nanowire structure with side facets that are mostly {100} with some {110} (schematic in Fig. 3b). Compared with Syn-CuNWs (Fig. 3b), A-CuNWs showed increasing percentage of A-(hkl) with prolonged activation time from 0% (0 h), 17% (0.5 h), 28% (1 h) to 41% (1.5 h) (Fig. 3f). Meanwhile, Cu{100} and Cu{110} were reduced from 67% to 39% and from 32% to 19%, respectively (Fig. 3f and Supplementary Table 1). These observations suggest that the {100} and {110} expressed on the Syn-CuNW surface gradually transformed into the higher-energy A-(hkl) surface structures during the electrochemical activation process, which is consistent with the TEM observations (Fig. 2).

Electrochemical CO_2RR evaluation. We studied the CO_2RR performance of CuNW catalysts with a gas-tight H-cell by analysing the effluent gases and liquid products at different applied potentials between −0.75 and −1.1 V in CO_2-saturated 0.1 M $KHCO_3$ (pH 6.8) at room temperature and under atmospheric pressure. The current density (j) and ECSA of the CuNWs were evaluated using the rotating disk electrode, the CO_2RR performances were evaluated in the H-cell coupled with gas chromatography barrier ionization discharge (GC-BID) (see the Methods for details). The performance of the A-CuNW catalysts was compared with those of commercial Cu foil and Syn-CuNWs (Fig. 4a–c). As most of the products from CO_2RR on our catalysts were in the gas phase, we focus our discussions of the CO_2RR performances on gas-phase products (Supplementary Tables 2–4). First, we observed that the A-CuNWs (with one hour activation) showed a considerably higher yield of C_2H_4 with an average peak $FE_{C_2H_4}$ of 69.79 ± 1.44% at around −1.00 V (Fig. 4c and Supplementary Table 2), when compared with the Syn-CuNWs ($FE_{C_2H_4}$ = 44.65 ± 2.20%) (Fig. 4b and Supplementary Table 3) and the polycrystalline Cu foil ($FE_{C_2H_4}$ = 22.80 ± 4.60%). We note that the primary CO_2RR products of the polycrystalline Cu foil were found to be CH_4 (24.67 ± 5.15%) and C_2H_4 (22.80 ± 4.60%) around −1.04 V (Supplementary Table 4), which is consistent with a previously reported CO_2RR of Cu polycrystalline foil[36].

Overall, compared with Syn-CuNWs, the A-CuNWs showed a higher partial current density of $FE_{C_2H_4}$ and a much lower HER partial current density (Supplementary Fig. 9). It has been reported that a high surface roughness could lead to enhanced C_2H_4 production[12], so we further compared the $FE_{C_2H_4}$ between commercial 25 nm Cu NPs and the A-CuNWs. We found that A-CuNWs showed less surface roughness, but still exhibited a $FE_{C_2H_4}$ about 30% higher

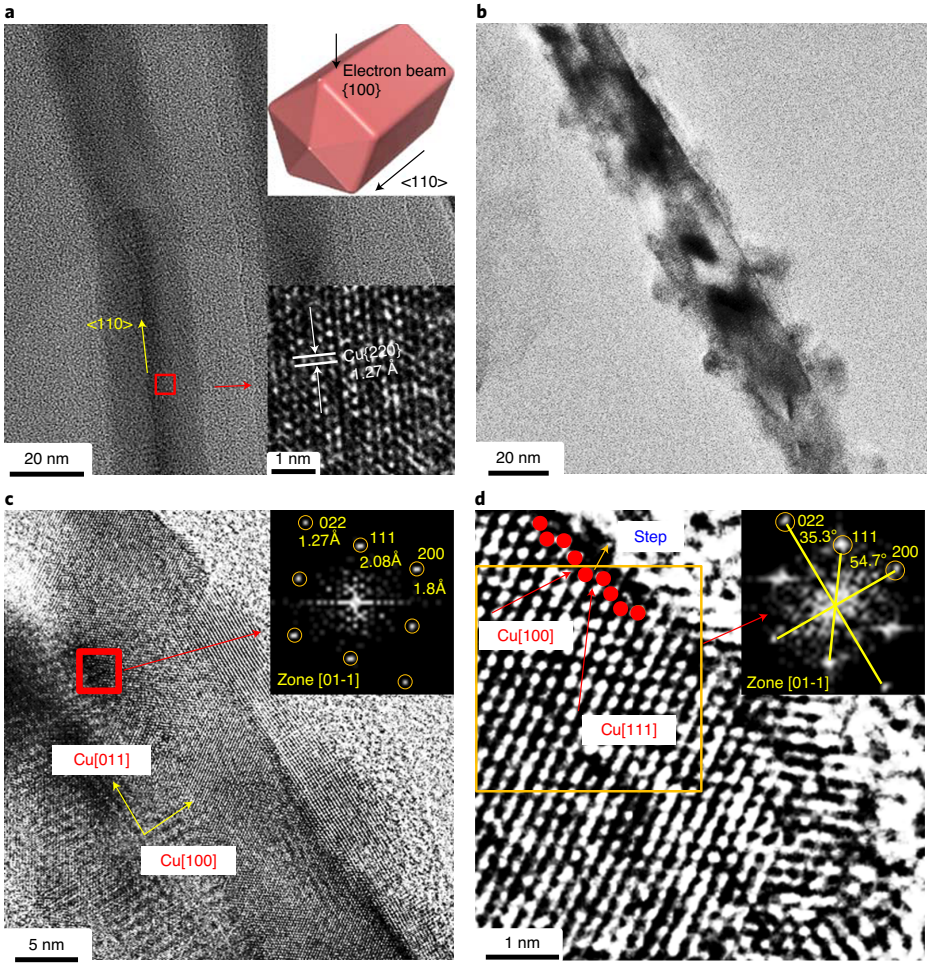

Fig. 2 | TEM characterizations of the Syn-CuNW and A-CuNW. a, Low magnification TEM image of Syn-CuNWs. Insets: schematic illustration (top) and HRTEM (bottom) of a Syn-CuNW showing the electron beam direction, <110> nanowire axial growth direction and expressed {100} side facets. **b**, Low-magnification TEM image of A-CuNW. **c**, HRTEM image of A-CuNW. Inset: FFT of the corresponding Cu phase, which indicates the <110> axial direction and expression of the {100} planes on the side surface. **d**, HRTEM image of an A-CuNW surface indicating the step structure. Inset: FFT from yellow box.

than that of the commercial 25 nm Cu NPs (37.08 ± 6.87% $FE_{C_2H_4}$ at −1.00 ± 0.01 V) (Supplementary Fig. 10), which rules out the likely contribution from the sample surface roughness to product selectivity. Hence, we tentatively attribute the high C_2H_4 selectivity observed in A-CuNWs to their highly stepped surface.

To further confirm the correlation between $FE_{C_2H_4}$ and the stepped-surface structure A-(*hkl*), we further compared different products from A-CuNWs with different activation durations and thus different surface portions of A-(*hkl*). Indeed, a clear correlation was observed between $FE_{C_2H_4}$ and A-(*hkl*). Specifically, as the stepped surface A-(*hkl*) gradually increased from 0 to 40.68%, the $FE_{C_2H_4}$ correspondingly increased from 47.04 to 71.19% (Fig. 4d). At the same time, we observed decreasing FE_{CH_4} and FE_{H_2} values with increasing A-(hkl) (Fig. 4d).

Importantly, these A-CuNWs with stepped surfaces exhibited a sustained high CO_2RR performance during the stability test. The A-CuNWs showed stable C_2H_4 production (61–72% $FE_{C_2H_4}$) for 205 hours at the corrected potentials ranging from −0.97 to −1.07 V (Fig. 4e). In comparison, the Cu foil only showed stability for less than two hours with ~20–34% FE_{CH_4} at −1.07 V (Supplementary Fig. 11). A repeated stability test that lasted 198 hours further confirmed the sustainable high performance of A-CuNWs with 64–79% $FE_{C_2H_4}$ (Supplementary Fig. 12). The sustained high $FE_{C_2H_4}$ suggested a high stability of the A-(*hkl*) surface steps on A-CuNWs. Indeed, the OH_{ad} spectra of A-CuNWs showed that the A-(*hkl*) portion remained at a stable range within 45.40 ± 5.62% for ~200 hours after the initial activation period (~1.5 hours) (Supplementary Fig. 13a). We also observed that during the stability test, the A-(*hkl*) continued to increase slightly with the ongoing CO_2RR after the initial 1.5 hours of activation (Supplementary Fig. 13b,c), correspondingly led to a further increase in $FE_{C_2H_4}$ (Supplementary Fig. 13d). The highest $FE_{C_2H_4}$ (79%) was hence achieved around 24 hours into the reaction during the stability test, which corresponded to an A-(*hkl*) of around 50% (Supplementary Figs. 12 and 13). Averaging over 16 FE measurements during the stability tests at a potential of around −1 V, we obtained a remarkably high $FE_{C_2H_4}$ of ~77.40 ± 3.16% (Table 1). Additionally, the SEI images confirmed that the A-CuNWs retained their one-dimensional morphology and stepped surface topology after the long-term stability tests (Supplementary Fig. 14). Together, the A-CuNWs demonstrated a remarkably high $FE_{C_2H_4}$ while maintaining their exceptional stability for 200 hours of continuous operation in a H-cell (Table 1 and Supplementary Table 5).

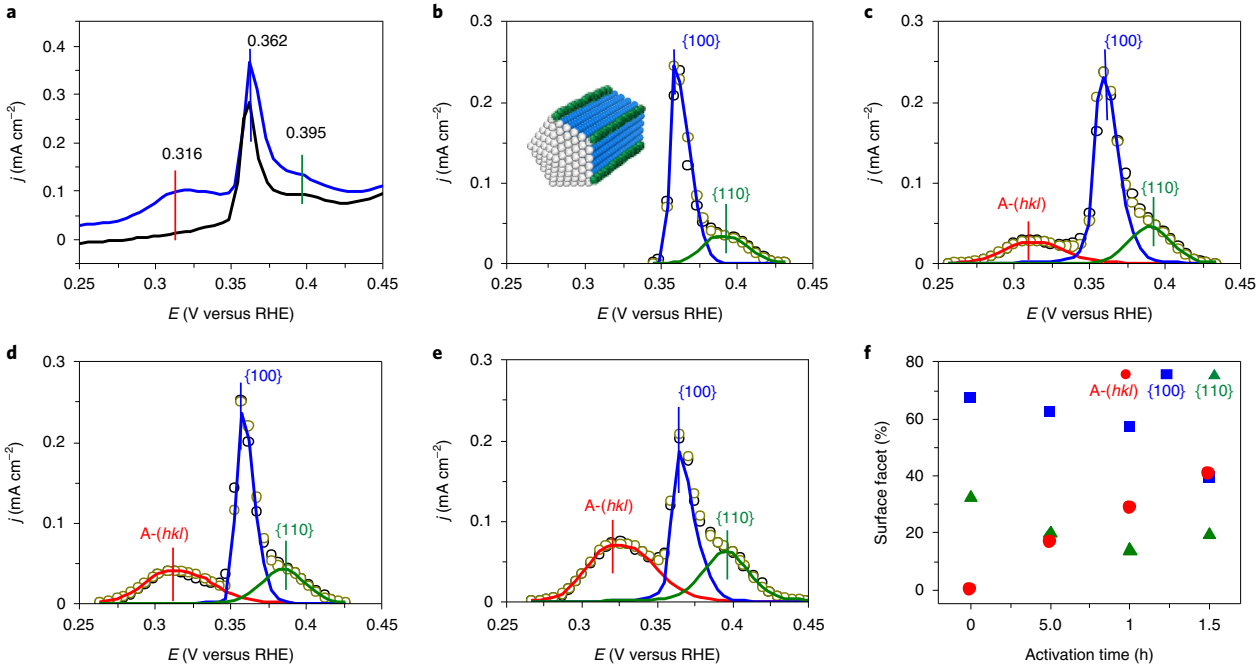

Fig. 3 | Electrochemical characterization of the surfaces of the CuNWs. a, Redox reactions of Syn-CuNWs (black) and A-CuNWs (blue) in 0.1 M KOH. **b–e**, Fitted OH^- adsorption peaks of Syn-CuNWs (**b**) (inset: schematic of the corresponding Syn-CuNW structure) and A-CuNWs with different activation durations, 0.5 h (**c**), 1 h (**d**) and 1.5 h (**e**). Peaks of different colour represent different facets on the nanowire surfaces. Blue, {100} facets; green, {110} facets; red, A-(*hkl*) (steps); black open circles, original data; yellow open circles, fitted data. **f**, Correlation between the portion of the surface facet and the activation duration on A-CuNW surfaces, showing an increasing A-(*hkl*) with longer activation.

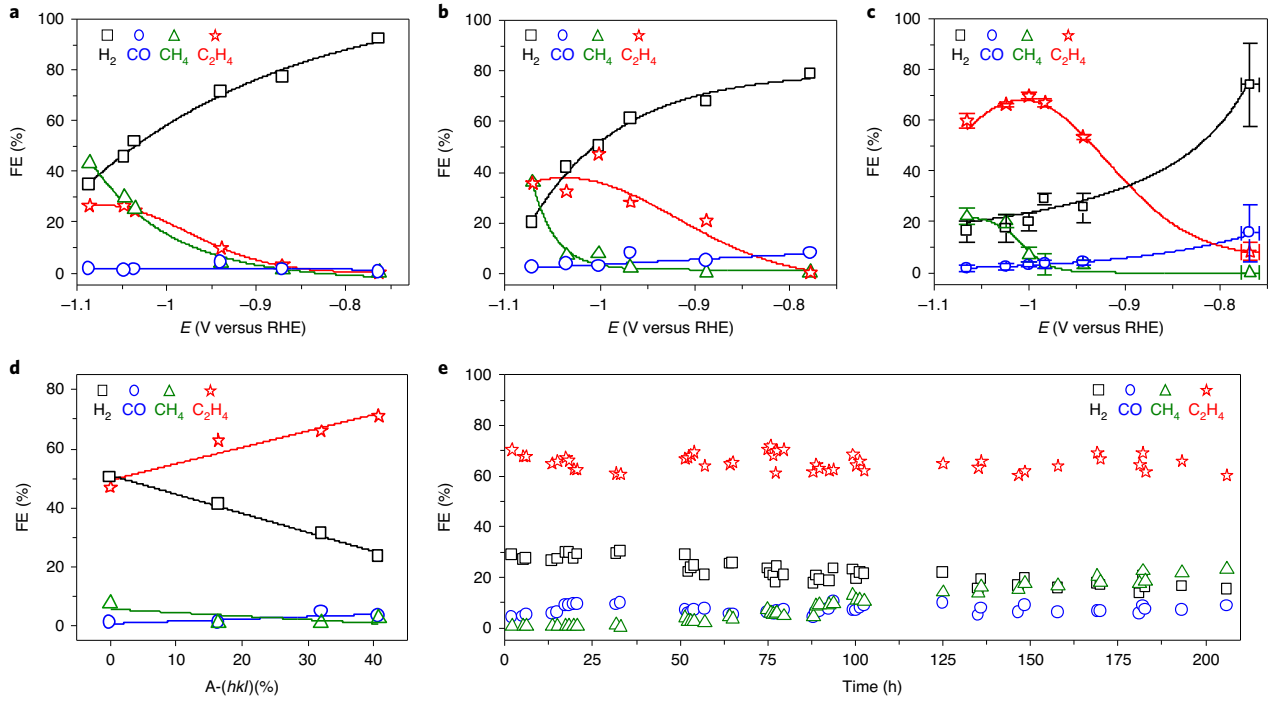

Fig. 4 | Electrochemical CO_2RR performance. a, FEs of Cu foil. **b**, FEs of Syn-CuNWs. **c**, FEs of A-CuNWs. Error bars in the *y* direction are the standard deviation (s.d.) of each FE; error bars in the *x* direction are the s.d. of the iR-corrected potential. Each error bar was calculated from three independent measurements. **d**, Correlation between A-(*hkl*) and FEs at about −0.99 to −1.00 V (RHE). **e**, Stability test of A-CuNW catalysts at corrected potentials, which range from about −0.97 to about −1.07 V (RHE).

Table 1 | Comparison of CO_2RR in peak C_2H_4 production for different Cu-based catalysts in H-cells

Catalysts	Applied potentials (V versus RHE)	$J_{C_2H_4}$ (mA cm^{-2})	Maximum $FE_{C_2H_4}$ (%)	Electrolyte	CO_2 flow rate (sccm)	Reference
A-CuNWs	−1.01 ± 0.01	~17.3	77.40 ± 3.16	0.1 M $KHCO_3$	15	This work
Cu nanocube (250–300 nm)	−0.95	11.2	45	0.1 M $KHCO_3$	20	54
Cu nanocube (10–40 nm)	~−0.86	6.7	33	0.1 M $KHCO_3$	20	55
Plasma-treated Cu foil	−0.90	7.2	60	0.1 M $KHCO_3$	30	14
Electro-redeposited Cu	−1.20	22.2	38	0.1 M $KHCO_3$	20	56
Branched CuO NPs	−1.05	~17.0	~70	0.1 M $KHCO_3$	60	57
Cu-based NPs	−1.10	~10.0	57	0.1 M $KHCO_3$	20	58

The $FE_{C_2H_4}$ of A-CuNWs is the average from 16 measurements in the stability tests.

DFT studies of surface stability and activity. The observation of a long-term stability of the high-index A-(*hkl*) surface is rather counterintuitive and intriguing, as high-energy surface steps were generally believed to be less stable than the low-index ones. To this end, we sought to assess the stability of the stepped surface under the working conditions. We performed grand canonical DFT calculations based on the Cu(S) [n(100)×m(111)] stepped surface to construct the surface phase diagram. Figure 5a,b shows the surface energies for Cu(100), Cu(111) and Cu(511) ([3(100)×(111)]) as a function of RHE potential. On Cu(100), we found one monolayer (ML) of hydrogen (H) for $U<-0.07$ V and 2 ML H for $U<-0.83$ V for equilibrium H coverage (θ_H). On Cu(511), we found 1 ML H for $U<-0.10$ V, 1.33 ML H for $U<-0.74$ V and that a further increase of H* evokes a severe surface reconstruction. On Cu(111), 1 ML H ($U<-0.08$ V) is the maximum coverage, which allows a local minimum of H* without any imaginary frequency. At $U=-0.98$ to -1.06 V, Cu(511) with $\theta_H=1.33$ has the lowest surface energy compared with Cu(100) at $\theta_H=2$ and Cu(111) at $\theta_H=1$ in (Fig. 5a,b). Therefore, we expect that once the stepped surface is formed, there is no driving force to reconstruct back to the flat Cu(100) surface at the working potential, which provides a good stability for the stepped surfaces.

We also calculated CO adsorption free energies to verify if the stepped surface is beneficial for CO adsorption, as the CO population is a key factor for C_{2+} products. We found that the step on Cu(511) leads to a 0.17 eV higher affinity for a single CO adsorption compared with that of Cu(100), as shown in Fig. 5c and Table 2. Moreover, the two adjacent molecular CO adsorptions can occur cooperatively, which is 0.44 eV more stable on the step sites on Cu(511) compared with those on Cu(100), where the c(2×2)-CO adlayer structure was observed in an operando scanning tunneling microscopy study[37]. Therefore, we confirmed that the step on Cu(511) can secure a higher local CO surface population, and that this facet is also favourable for two adjacent CO adsorptions, which is beneficial for C–C coupling.

Next, we performed DFT to explain the reaction kinetics. The OCCHO* intermediate is an important intermediate towards the production of C_2 products, especially at higher overpotentials[38,39], whereas the HCO* intermediate can branch out to form either HCOH* for the C_1 pathway or OCCHO* for the C_2 pathway (Fig. 5d–f). We calculated the reaction energy barriers ($\Delta G^{\ddagger}$) and reaction free energies (ΔG) for each pathway, as shown in Table 2. The frequency contributions are listed in Supplementary Table 6. To calculate the kinetic barrier for the protonation of the HCO* intermediate into HCOH*, we introduced a surface water molecule as a proton source at pH 6.8. The reduction of HCO* to HCOH* occurs with $\Delta G^{\ddagger}=0.53$ eV on Cu(100) and $\Delta G^{\ddagger}=0.59$ eV on Cu(511), respectively. Therefore, Cu(511) has a 0.06 eV higher reaction barrier from HCO* to HCOH*, which makes it about ten times slower than that on Cu(100) at 298 K. However, despite the high stability of the 2CO* configuration, the kinetic barrier for C–C coupling from CO* + HCO* towards OCCHO* (C_2 pathway) on Cu(511) is only 0.02 eV higher than that on Cu(100), which makes it only two times slower than that on Cu(100). We also performed DFT calculations for the hydrogen binding energy (HBE) on Cu(100) and on various adsorption sites on Cu(511) to estimate the HER activity based on the fact that a low HER activity for Cu has been attributed to its weak HBE[40]. Compared with the HBE of −0.31 eV on Cu(100), Cu(511) showed even smaller HBEs that ranged from −0.06 to −0.29 eV on various binding sites (Supplementary Fig. 15), which indicates the suppression of HER on Cu(511).

Thus, we suggest that the high local population of 2CO*, the higher barrier for the C_1 path on Cu(511) and the slower HER are the key factors that underlie the enhancement in C_2 production observed on A-CuNWs. These results are all consistent with the experimental observations that an increasing surface ratio of the stepped surface A-(*hkl*) led to an increase $FE_{C_2H_4}$, and decrease in both FE_{CH_4} and FE_{H_2} (Fig. 4d and Supplementary Fig. 13b,c). In addition, the stronger OH^- adsorption on A-CuNWs can also induce longer H_2O adsorption residence times on the surface of Cu, which leads to the preference of hydrocarbon products (for example, C_2H_4) over alcohol products (for example, ethanol), which share a common intermediate with C_2H_4 (refs. [41,42]). This is consistent with the observed low ethanol production for A-CuNW catalysts (Supplementary Table 2).

Discussion

In conclusion, we report here that CuNW catalysts with a highly stepped surface exhibit a high $FE_{C_2H_4}$ (77.40 ± 3.16%) that is stable for ~200 hours in H-cells. Coupled with structural and electrochemical surface characterizations of A-CuNWs, our DFT calculations showed that the stepped surface [3(100)×(111)]) exhibits a high local population of 2CO* and a higher barrier for the C_1 path compared with that for Cu(100), which leads to a higher product selectivity towards C_2H_4. These findings suggest an effective approach to engineer catalyst surfaces for high reactivity, high selectivity and high stability under operando conditions.

Methods

Chemicals. Copper(II) chloride dihydrate ($CuCl_2{\cdot}2H_2O$, 99.999%), D-(+)-glucose (>99.5%), hexadecylamine (>98%), ethanol (200 proof) and 25 nm Cu NPs were all purchased from Sigma-Aldrich. KOH and hexane (99.9%) were purchased from Fisher Chemical. All the chemicals were used without purification. An ultrapure purification system (Milli-Q advantage A10) produced the deionized water (18.2 MΩ cm) used to make the solutions. The 99.9% Cu foil obtained from Metal Remnants, Inc. was cut to 1 cm^2 and mechanically polished by 400G sandpaper from 3M and electrochemically polished in 85% phosphoric acid under −1 V (RHE) for 5 min. The Cu foil was subsequently rinsed with deionized water and used for CO_2RR.

Preparation of CuNW catalysts. In a typical synthesis of the CuNW catalysts, 22 mg of $CuCl_2{\cdot}2H_2O$, 50 mg of D-(+)-glucose and 180 mg of hexadecylamine were predissolved in 10 ml of deionized water in a 30 ml vial. The chemical solution

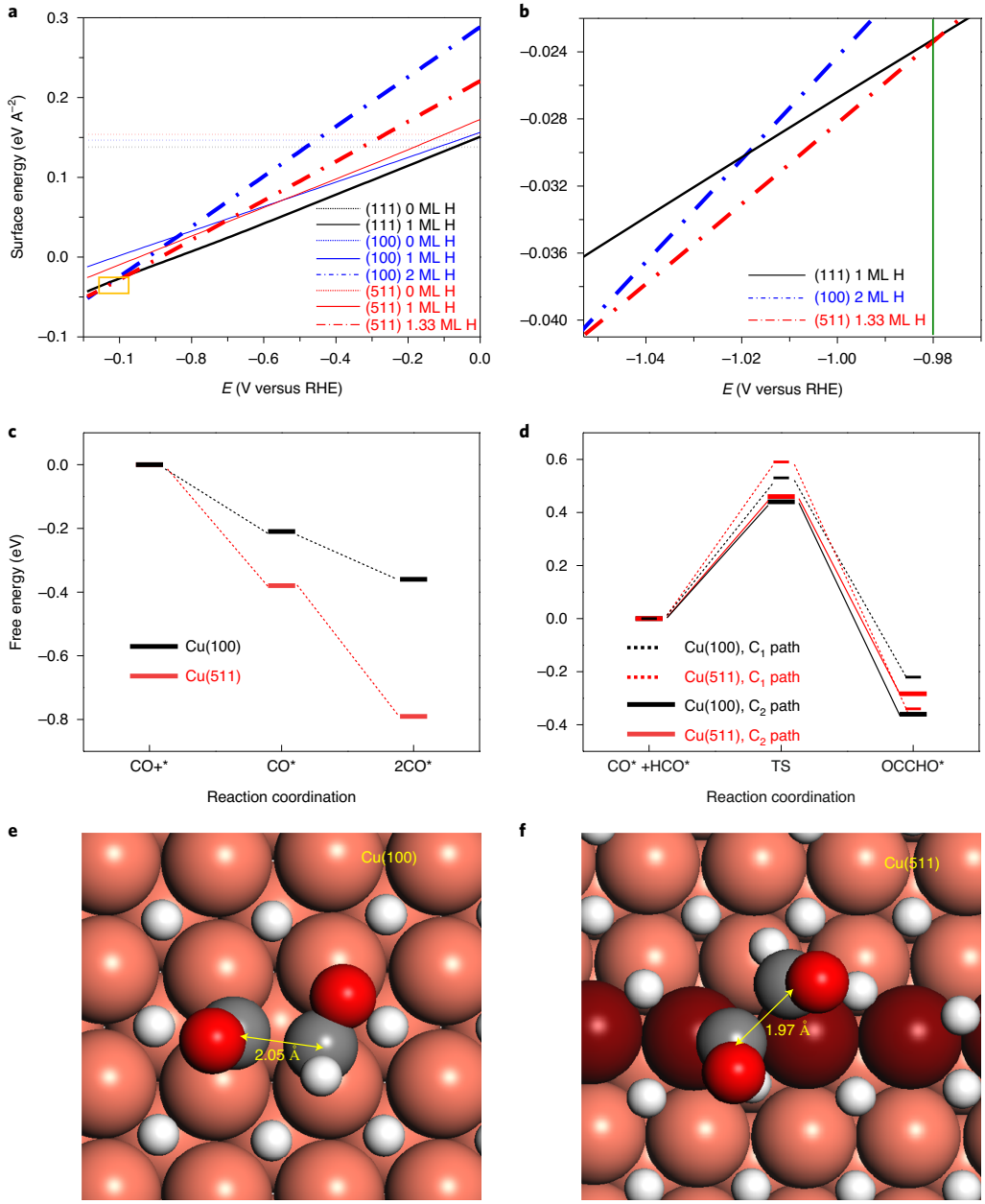

Fig. 5 | The stability and activity of the Cu(511) step surface. a, Surface phase diagram of Cu(100) and Cu(511) ([3(100)×(111)]) for 0 ML, 1 ML H and the highest stabilized H coverages as a function of potentials at pH 7. **b**, Magnified view of the yellow box in **a**. **c**, CO and 2CO adsorption energies (ΔG_{ads}) on Cu(100) and Cu(511). The CO+* represents CO and an active site on the surface before the adsorption of CO; the CO* represents the active site with CO adsorption. **d**, C_1 and C_2 pathways on Cu(100) and Cu(511). **e**,**f**, Transition states (TS) for the C_2 pathway on Cu(100) (**e**) and Cu(511) (**f**). Orange, Cu; grey, C; red, O; white, H.

was mixed under sonication for 15 min and then transferred to an oil bath. The mixture was heated from room temperature to 100 °C for 8 h and cooled to room temperature. The Syn-CuNWs were washed five times with sonication in a hexane/ethanol (1:1 volume) solvent for 20 min. The CuNWs were collected by centrifuge at 9,500 rpm.

Characterization of materials. A hexane dispersion of the catalysts was dropped onto and dried on carbon-coated copper TEM grids (Ted Pella) at room temperature to prepare the TEM samples. A FEI CM120 TEM at 120 kV was used for low-resolution TEM images. A FEI Titan TEM operating at 300 kV was used to take the HRTEM images. Dark-field scanning transmission electron microscopy images were taken by a JEM-ARM300F Grand ARM TEM at 300 kV. Scanning electron microscopy (SEM) images were taken by Nova Nano 230, and SEI was taken by JEOL 2800 TEM with 200 kV. The size of the CuNWs was measured by the largest diameter within the CuNWs. The size was determined by averaging more than 100 nanowires. A Panalytical X'Pert Pro X-ray powder diffractometer with Cu Kα radiation was used for the powder X-ray diffraction patterns. Inductively coupled plasma atomic emission spectroscopy (TJA RADIAL IRIS 1000) was conducted to determine the metal concentration in the catalysts used.

Electrode preparation and collecting data for the calculation of FE. Dried CuNWs (4 mg) were mixed with 1 ml of ethanol, followed by ultrasonication for 1 h. Subsequently, 10 µl of Nafion (5 wt%) was added and ultrasonication continued for an extra 10 min. The catalyst ink (10 µl) was dropped onto the electrodes using

Table 2 | CO ΔG_{ads}, $\Delta G^{\ddagger}$ and ΔG for C_1 and C_2 pathways by 1 ML of H*

	1CO*	2CO*	HCO* → HCOH*		CO* + HCO* → OCCHO*	
	ΔG_{ads} (eV)	ΔG_{ads} (eV)	$\Delta G^{\ddagger}$ (eV)	ΔG (eV)	$\Delta G^{\ddagger}$ (eV)	ΔG (eV)
Cu(100)	−0.21	−0.36	0.53	−0.22	0.44	−0.36
Cu(511)	−0.38	−0.80	0.59	−0.34	0.46	−0.28

a pipette and dried under ambient air. The 10 µl of the catalyst ink contained 0.04 mg of Cu, quantified by inductively coupled plasma atomic emission spectroscopy.

To activate the CuNW catalysts and measure FE, a gas-tight electrolysis H-cell (WizMac) separated with a Nafion ion exchange membrane (Sigma Aldrich) was used. The working electrode coated with catalysts was an L-type glassy-carbon electrode (diameter, 5 mm; area, 0.196 cm^2) from WizMac. A Pt coil from Pine Instruments was used as a counter electrode. A 4 M KCl Ag/AgCl electrode from Pine Instruments was used as a reference electrode. The impedance of each solution was tested on a Princeton VersaSTAT 4 electrochemical workstation. After iR correction, all potentials were converted into those against RHE.

A 0.1 M $KHCO_3$ electrolyte solution was used for all electrochemical CO_2RR. Before CO_2RR, we bubbled CO_2 (Airgas, 99.99%) for 30 min to reach saturation, and we kept purging CO_2 into the cathodic compartment at 15 sccm with stirring at 1,200 r.p.m. during the CO_2RR. The activation of the CuNW catalysts was conducted with chronoamperometry in a CO_2-saturated 0.1 M $KHCO_3$ solution at −1.05 V (RHE) for 1 h. We measured the FE by using chronoamperometry for 30–40 min at each applied potential except for the Syn-CuNW catalysts. The FEs of Syn-CuNW catalysts were measured in 10 min to prevent any activation of the CuNW catalysts (Supplementary Fig. 7). For the long-term stability test, the CO_2-saturated 0.1 M $KHCO_3$ electrolyte was replaced every 12 h and pulse potentials (about −0.97 V (RHE) for 600 s and 0.32 V (RHE) for 10 s) were applied to remove possible surface poisoning from the produced formate[43,44]. The FEs were measured roughly every 2–3 h during the stability test, except for during the night shift. The stability test was performed at room temperature and under atmospheric pressure.

Gas product analysis was done with a Shimadzu Tracera GC-BID 2010 Plus (Shimadzu) equipped with a Restek Micropacked GC column. The standard curve of the GC-BID was calibrated with five standard gases (Airgas). The carrier gas was helium (Airgas, 99.9999%). A p-type Hastelloy six port sampling loop (1.5 ml) was directly routed to an outlet gas line of a gas-tight H-cell. The effluence gas (1.5 ml) was analysed with the Shimadzu Tracera GC-BID 2010 Plus. The FE was calculated as[45]:

$$FE_J = \frac{2Fv_J G_{FR} p_0}{RT_0 i_{total}} \times 100\% \quad (1)$$

where v_J (vol%) is the volume concentration of gas products (J = CO, CH_4, C_2H_4 or H_2) in the effluence gas from the electrochemical cell (gas chromatography data), G_{FR} (ml min^{-1} at room temperature and ambient pressure) is the gas flow rate measured by a ProFlow 6000 electronic flow meter (Restek) at the exit of the electrochemical cell, i_{total} (mA) is the steady-state cell current, pressure is $p_0 = 1.01 \times 10^5$ Pa, temperature $T_0 = 298.15$ K, Faraday constant $F = 96{,}485$ C mol^{-1} and gas constant $R = 8.314$ J mol^{-1} K^{-1}.

Quantitative NMR spectroscopy (Bruker AV-600) was conducted to analyse the liquid products. Specifically, 0.3 ml of D_2O was added to 0.65 ml of the reacted electrolyte, and 50 µl of dimethyl sulfoxide (0.512 µM ml^{-1}) was also mixed in as an internal standard. The one-dimensional ^{1}H spectrum was measured with a prewater saturation method.

Electrochemical measurements. Before we carried out OH_{ad} on CuNWs, the CuNWs on the L-type glassy-carbon electrode were activated in a H-cell with CO_2-saturated 0.1 M $KHCO_3$ by purging CO_2 gas. Then, the catalysts on the L-type glassy-carbon electrode were transferred to a three-electrode cell.

For the OH^- adsorption reaction, we conducted OH^- adsorption reaction CV in 0.1 M KOH at a 100 mV s^{-1} scan rate with Hg/HgO as the reference electrode (CH Instruments). The OH^- adsorption reaction is described accurately by one electron process as the following[33]:

$$Cu^* + OH^- \leftrightarrow Cu^*(OH)_{ad} + e^- \quad (2)$$

$$Cu + OH^- \leftrightarrow Cu(OH)_{ad} + e^- \quad (3)$$

To calculate the number of OH^- adsorptions on each Cu plane on the CV scan, the linear background was subtracted[30]. We integrated current that corresponds to the assigned Cu{100}, Cu{110} and Cu{111} facets and A-(*hkl*) by each peak scan time as follows:

$$\frac{\int I dV}{v \times e} = \text{the number of OH adsorptions on Cu facets} \quad (4)$$

where I (C s^{-1}) is the current under the OH^- absorption peak that corresponds to each Cu facet, dV (V) is the corresponding voltage, v (V s^{-1}) is the scan rate of the OH^- adsorption CV scan and e is the electric charge (1.602×10^{-19} C).

For the total current densities and ECSA measurements, a three-electrode cell was used. The working electrode was a glassy-carbon rotating disk electrode (diameter, 5 mm; area, 0.196 cm^2) from Pine Instruments and coated with catalysts. A graphite rod was used as the counter electrode. The double junction Ag/AgCl (the inner filling 4 M KCl and the outer filling 10% KNO_3) electrode from Pine Instruments was the reference electrode. The total current densities were measured from CV scans between 0 V and −1.1 V (RHE) at 50 mV s^{-1} with a rotating disk electrode at 1,200 r.p.m. in CO_2-saturated 0.1 M $KHCO_3$. Subsequently, ECSAs of the CuNWs were measured by Pb under a potential deposition. The background current was measured in N_2-saturated 0.1 M $HClO_4$ between 0.26 V and −0.38 V (RHE) at 10 mV s^{-1}. In a N_2-saturated 0.1 M $HClO_4$ + 0.001 M $Pb(ClO_4)_2$ solution at room temperature, ECSA measurements were carried out by subtracting the background current from the integrated Pb desorption charge on the CV between 0.26 V and −0.38 V (RHE) at 10 mV s^{-1} (refs. [28]). A conversion factor of 310 µC cm^{-2} was based on a monolayer of Pb adatom coverage over Cu and 2e$^-$ Pb oxidation[28].

Computational details for Cu(100) and Cu(511). The quantum mechanics calculations were carried out using the VASP software version 5.4.4[46–48] with the Perdew–Burke–Ernzerhof flavour[49] of DFT. The projector augmented wave method[50] was used to account for core–valence interactions. The kinetic energy cutoff for plane-wave expansions was set to 500 eV, and reciprocal space was sampled by the Monkhorst–Pack scheme with a grid of 3 × 3 × 1 and 2 × 3 × 1 for Cu(100) and Cu(511), respectively. The vacuum layer was at least 20 Å above the surface. The convergence criteria were 1×10^{-5} eV energy differences to solve the electronic wave function. Methfessel–Paxton smearing of second order with a width of 0.1 eV was applied. All the geometries (atomic coordinates) were converged to within 0.03 eV $Å^{-1}$ for the maximal components of forces. A poststage vdW DFT-D3 method with Becke–Jonson damping was applied[51]. The solvation was treated implicitly using the VASPsol[52] method.

We employed climbing image nudged elastic band method[53] with five images to find the potential energy surface along with the reaction coordinates, and the subsequent dimer method was applied near the saddle point to find the transition state until the force converges to <0.01 eV $Å^{-1}$. All the transition states had only one imaginary frequency.

All Gibbs free energy (G) values include the vibrational contributions of zero-point vibrational energy (E_{ZPE}), enthalpy (H) and entropy (S). To compare all the surfaces, we normalized the Gibbs free energy to its surface area. The Gibbs free energies were calculated at 298 K and 1 atm, as in:

$$G = H - T\Delta S = E_{DFT} + E_{ZPE} + E_{solv} + \int_0^{298} C_v dT - T\Delta S \quad (5)$$

where E_{DFT} is the DFT-optimized total energy, E_{solv} is the solvation energy, $\int_0^{298} C_v dT$ is the heat capacity and T is the temperature.

For the surface phase diagram, the Gibbs free energy change was calculated at 298 K, pH 7, as in:

$$\Delta G_{surf} = G_{surf-sol} - G_{bulk-sol} - NG_{H_2O-sol} + n\left(\frac{1}{2}G^{\circ}_{H_2} + k_B T \ln a_{H^+} - eU\right) \quad (6)$$

where k_B is the Boltzmann constant, a_{H+} is the proton activity and U is the applied potential.

Structures. The atomic coordinates of the optimized computational models are all provided as a text file in Supplementary Data 1.

Data availability

The data that support the findings of this study are available from the corresponding authors upon reasonable request.

Received: 8 July 2019; Accepted: 30 July 2020;
Published online: 7 September 2020

References

1. Schreier, M. et al. Solar conversion of CO_2 to CO using Earth-abundant electrocatalysts prepared by atomic layer modification of CuO. *Nat. Energy* **2**, 17087 (2017).
2. Hori, Y., Wakebe, H., Tsukamoto, T. & Koga, O. Electrocatalytic process of CO selectivity in electrochemical reduction of CO_2 at metal electrodes in aqueous media. *Electrochim. Acta* **39**, 1833–1839 (1994).

3. Hori, Y., Kikuchi, K. & Suzuki, S. Production of CO and CH_4 in electrochemical reduction of CO_2 at metal electrodes in aqueous hydrogen carbonate solution. *Chem. Lett.* **14**, 1695–1698 (1985).
4. Qiao, J., Liu, Y., Hong, F. & Zhang, J. A review of catalysts for the electro-reduction of carbon dioxide to produce low-carbon fuels. *Chem. Soc. Rev.* **43**, 631–675 (2014).
5. Gawande, M. B. et al. Cu and Cu-based nanoparticles: synthesis and applications in catalysis. *Chem. Rev.* **116**, 3722–3811 (2016).
6. Kim, D., Resasco, J., Yu, Y., Asiri, A. M. & Yang, P. Synergistic geometric and electronic effects for electrochemical reduction of carbon dioxide using gold–copper bimetallic nanoparticles. *Nat. Commun.* **5**, 4948 (2014).
7. Lu, Q. et al. A selective and efficient electrocatalyst for carbon dioxide reduction. *Nat. Commun.* **5**, 3242 (2014).
8. Mistry, H., Varela, A. S., Kühl, S., Strasser, P. & Cuenya, B. R. Nanostructured electrocatalysts with tunable activity and selectivity. *Nat. Rev. Mater.* **1**, 16009 (2016).
9. Angamuthu, R., Byers, P., Lutz, M., Spek, A. L. & Bouwman, E. Electrocatalytic CO_2 conversion to oxalate by a copper complex. *Science* **327**, 313–315 (2010).
10. Li, Y. et al. Structure-sensitive CO_2 electroreduction to hydrocarbons on ultrathin 5-fold twinned copper nanowires. *Nano Lett.* **17**, 1312–1317 (2017).
11. Cheng, T., Xiao, H. & Goddard, W. A. III Reaction mechanisms for the electrochemical reduction of CO_2 to CO and formate on the Cu(100) surface at 298 K from quantum mechanics free energy calculations with explicit water. *J. Am. Chem. Soc.* **138**, 13802–13805 (2016).
12. Raciti, D., Mao, M., Park, J. H. & Wang, C. Local pH effect in the CO_2 reduction reaction on high-surface-area copper electrocatalysts. *J. Electrochem. Soc.* **165**, F799 (2018).
13. Li, C. W. & Kanan, M. W. CO_2 reduction at low overpotential on Cu electrodes resulting from the reduction of thick Cu_2O films. *J. Am. Chem. Soc.* **134**, 7231–7234 (2012).
14. Mistry, H. et al. Highly selective plasma-activated copper catalysts for carbon dioxide reduction to ethylene. *Nat. Commun.* **7**, 12123 (2016).
15. Choi, C. et al. A highly active star decahedron Cu nanocatalyst for hydrocarbon production at low overpotentials. *Adv. Mater.* **31**, 1805405 (2019).
16. Feng, X., Jiang, K., Fan, S. & Kanan, M. W. Grain-boundary-dependent CO_2 electroreduction activity. *J. Am. Chem. Soc.* **137**, 4606–4609 (2015).
17. Li, C. W., Ciston, J. & Kanan, M. W. Electroreduction of carbon monoxide to liquid fuel on oxide-derived nanocrystalline copper. *Nature* **508**, 504–507 (2014).
18. Mariano, R. G., McKelvey, K., White, H. S. & Kanan, M. W. Selective increase in CO_2 electroreduction activity at grain-boundary surface terminations. *Science* **358**, 1187–1192 (2017).
19. Favaro, M. et al. Subsurface oxide plays a critical role in CO_2 activation by Cu(111) surfaces to form chemisorbed CO_2, the first step in reduction of CO_2. *Proc. Natl Acad. Sci. USA* https://doi.org/10.1073/pnas.1701405114 (2017).
20. Lum, Y. & Ager, J. W. Stability of residual oxides in oxide-derived copper catalysts for electrochemical CO_2 reduction investigated with ^{18}O labeling. *Angew. Chem. Int. Ed. Engl.* **57**, 551–554 (2018).
21. *Ethylene—Global Market Trajectory and Analytics* https://www.researchandmarkets.com/reports/354876/ethylene_global_market_trajectory_and_analytics (Research and Markets, 2020).
22. Cheng, T., Xiao, H. & Goddard, W. A. Full atomistic reaction mechanism with kinetics for CO reduction on Cu(100) from ab initio molecular dynamics free-energy calculations at 298 K. *Proc. Natl Acad. Sci. USA* **114**, 1795–1800 (2017).
23. Cheng, T., Xiao, H. & Goddard, W. A. Nature of the active sites for CO reduction on copper nanoparticles; suggestions for optimizing performance. *J. Am. Chem. Soc.* **139**, 11642–11645 (2017).
24. Hori, Y., Takahashi, I., Koga, O. & Hoshi, N. Selective formation of C2 compounds from electrochemical reduction of CO_2 at a series of copper single crystal electrodes. *J. Phys. Chem. B* **106**, 15–17 (2002).
25. Jin, M. et al. Shape-controlled synthesis of copper nanocrystals in an aqueous solution with glucose as a reducing agent and hexadecylamine as a capping agent. *Angew. Chem. Int. Ed.* **50**, 10560–10564 (2011).
26. Yang, H. J., He, S. Y. & Tuan, H. Y. Self-seeded growth of five-fold twinned copper nanowires: mechanistic study, characterization, and SERS applications. *Langmuir* **30**, 602–610 (2014).
27. Mandal, L. et al. Investigating the role of copper oxide in electrochemical CO_2 reduction in real time. *ACS Appl. Mater. Inter.* **10**, 8574–8584 (2018).
28. Baturina, O. A. et al. CO_2 electroreduction to hydrocarbons on carbon-supported Cu nanoparticles. *ACS Catal.* **4**, 3682–3695 (2014).
29. Droog, J. M. & Schlenter, B. Oxygen electrosorption on copper single crystal electrodes in sodium hydroxide solution. *J. Electroanal. Chem.* **112**, 387–390 (1980).
30. De Chialvo, M. G., Zerbino, J. O., Marchiano, S. L. & Arvia, A. J. Correlation of electrochemical and ellipsometric data in relation to the kinetics and mechanism of Cu_2O electroformation in alkaline solutions. *J. Appl. Electrochem.* **16**, 517–526 (1986).
31. Raciti, D. et al. Low-overpotential electroreduction of carbon monoxide using copper nanowires. *ACS Catal.* **7**, 4467–4472 (2017).
32. Luc, W. et al. Two-dimensional copper nanosheets for electrochemical reduction of carbon monoxide to acetate. *Nat. Catal.* **1**, 423–430 (2019).
33. De Chialvo, M. G., Marchiano, S. L. & Arvia, A. J. The mechanism of oxidation of copper in alkaline solutions. *J. Appl. Electrochem.* **14**, 165–175 (1984).
34. Zhang, S., Kang, P. & Meyer, T. J. Nanostructured tin catalysts for selective electrochemical reduction of carbon dioxide to formate. *J. Am. Chem. Soc.* **136**, 1734–1737 (2014).
35. Tian, F. H. & Wang, Z. X. Adsorption of an O atom on the Cu(311) step defective surface. *J. Phys. Chem. B* **108**, 1392–1395 (2004).
36. Hori, Y., Wakebe, H., Tsukamoto, T. & Koga, O. Adsorption of CO accompanied with simultaneous charge transfer on copper single crystal electrodes related with electrochemical reduction of CO_2 to hydrocarbons. *Surf. Sci.* **335**, 258–263 (1995).
37. Baricuatro, J. H., Kim, Y. G., Korzeniewski, C. L. & Soriaga, M. P. Seriatim ECSTM–ECPMIRS of the adsorption of carbon monoxide on Cu(100) in alkaline solution at CO_2-reduction potentials. *Electrochem. Commun.* **91**, 1–4 (2018).
38. Resasco, J. et al. Promoter effects of alkali metal cations on the electrochemical reduction of carbon dioxide. *J. Am. Chem. Soc.* **139**, 11277–11287 (2017).
39. Montoya, J. H., Shi, C., Chan, K. & Nørskov, J. K. Theoretical insights into a CO dimerization mechanism in CO_2 electroreduction. *J. Phys. Chem. Lett.* **6**, 2032–2037 (2015).
40. Seh, Z. W. et al. Combining theory and experiment in electrocatalysis: insights into materials design. *Science* **13**, 4998 (2017).
41. Yamamoto, S. et al. In situ X-ray photoelectron spectroscopy studies of water on metals and oxides at ambient conditions. *J. Phys. Condens. Matter* **20**, 184025 (2008).
42. Xiao, H., Cheng, T. & Goddard, W. A. III Atomistic mechanisms underlying selectivities in C_1 and C_2 products from electrochemical reduction of CO on Cu(111). *J. Am. Chem. Soc.* **139**, 130–136 (2016).
43. DeWulf, D. W., Jin, T. & Bard, A. J. Electrochemical and surface studies of carbon dioxide reduction to methane and ethylene at copper electrodes in aqueous solutions. *J. Electrochem. Soc.* **136**, 1686–1691 (1989).
44. Engelbrecht, A. et al. On the electrochemical CO_2 reduction at copper sheet electrodes with enhanced long-term stability by pulsed electrolysis. *J. Electrochem. Soc.* **165**, J3059–J3068 (2018).
45. Zhu, W. et al. Monodisperse Au nanoparticles for selective electrocatalytic reduction of CO_2 to CO. *J. Am. Chem. Soc.* **135**, 16833–16836 (2013).
46. Kresse, G., Furthmüller, J. & Hafner, J. Theory of the crystal structures of selenium and tellurium: the effect of generalized-gradient corrections to the local-density approximation. *Phys. Rev. B* **50**, 13181 (1994).
47. Kresse, G. & Furthmüller, J. Efficiency of ab-initio total energy calculations for metals and semiconductors using a plane-wave basis set. *Comput. Mater. Sci.* **6**, 15–50 (1996).
48. Kresse, G. & Furthmüller, J. Efficient iterative schemes for ab initio total-energy calculations using a plane-wave basis set. *Phys. Rev. B* **54**, 11169 (1996).
49. Perdew, J. P., Burke, K. & Ernzerhof, M. Generalized gradient approximation made simple. *Phys. Rev. Lett.* **77**, 3865 (1996).
50. Kresse, G. & Joubert, D. From ultrasoft pseudopotentials to the projector augmented-wave method. *Phys. Rev. B* **59**, 1758 (1999).
51. Grimme, S., Antony, J., Ehrlich, S. & Krieg, H. A consistent and accurate ab initio parametrization of density functional dispersion correction (DFT-D) for the 94 elements H–Pu. *J. Chem. Phys.* **132**, 154104 (2010).
52. Mathew, K., Sundararaman, R., Letchworth-Weaver, K., Arias, T. A. & Hennig, R. G. Implicit solvation model for density-functional study of nanocrystal surfaces and reaction pathways. *J. Chem. Phys.* **140**, 084106 (2014).
53. Henkelman, G. & Jónsson, H. Improved tangent estimate in the nudged elastic band method for finding minimum energy paths and saddle point. *J. Chem. Phys.* **113**, 9978 (2000).
54. Gao, D. et al. Plasma-activated copper nanocube catalysts for efficient carbon dioxide electroreduction to hydrocarbons and alcohols. *ACS Nano* **11**, 4825–4831 (2017).
55. Kim, D., Kley, C. S., Li, Y. & Yang, P. Copper nanoparticle ensembles for selective electroreduction of CO_2 to C_2–C_3 products. *Proc. Natl Acad. Sci. USA* **114**, 10560–10565 (2017).
56. De Luna, P. et al. Catalyst electro-redeposition controls morphology and oxidation state for selective carbon dioxide reduction. *Nat. Catal.* **1**, 103–110 (2018).
57. Kim, J. et al. Branched copper oxide nanoparticles induce highly selective ethylene production by electrochemical carbon dioxide reduction. *J. Am. Chem. Soc.* **141**, 6986–6994 (2019).
58. Jung, H. et al. Electrochemical fragmentation of Cu_2O nanoparticles enhancing selective C–C coupling from CO_2 reduction reaction. *J. Am. Chem. Soc.* **141**, 4624–4633 (2019).

Acknowledgements

The TEM work was conducted using the facilities in the Electron Imaging Center at the California NanoSystems Institute at the University of California Los Angles and the Irvine Materials Research Institute at the University of California Irvine. C.C., J.C., X.D. and Y.H. acknowledge support from the Office of Naval Research (ONR) under grant no. N000141712608. S.K., T.C. and W.A.G. were supported by the Joint Center for Artificial Photosynthesis, a DOE Energy Innovation Hub, supported through the Office of Science of the US Department of Energy under Award no. DE-SC0004993. C.L., S.K. and H.M.L. used the Extreme Science and Engineering Discovery Environment (XSEDE), which is supported by National Science Foundation grant no. ACI-1548562. C.L. and H.M.L. were also supported by a National Research Foundation (NRF) of Korea grant funded by the Korean Government (no. NRF-2017R1E1A1A03071049). The work done at the University of California Irvine was supported by the Irvine Materials Research Institute and ExxonMobil.

Author contributions

C.C. designed and conducted most of the experiments, analysed all the data and prepared the manuscript. S.K., T.C. and W.A.G. performed the density theoretical calculations and prepared the manuscript. M.X., P.T. and X.P. took SEI and bright-field scanning transmission electron microscopy images. J.C., C.L., H.M.L and X.D. assisted in the experiments and the preparation of the manuscript. Y.H. initiated the study, oversaw the project and wrote the manuscript. All the authors discussed the results and contributed to the manuscript.

Competing interests

The authors declare no competing interests.

Additional information

Supplementary information is available for this paper at https://doi.org/10.1038/s41929-020-00504-x.

Correspondence and requests for materials should be addressed to W.A.G. or Y.H.

Reprints and permissions information is available at www.nature.com/reprints.

Publisher's note Springer Nature remains neutral with regard to jurisdictional claims in published maps and institutional affiliations.